

# **Lithographic characterization of the printability of programmed EUV substrate defects**

Patrick Naulleau,<sup>1</sup> Kenneth A. Goldberg,<sup>1</sup> Erik H. Anderson<sup>1</sup>, Jeffrey Bokor<sup>1,2</sup>, Eric Gullikson<sup>1</sup>, Bruce Harteneck<sup>1</sup>, Keith Jackson<sup>1</sup>, Deirdre Olynick<sup>1</sup>, Farhad Salmassi<sup>1</sup>, Sherry Baker<sup>2</sup>, Paul Mirkarimi<sup>2</sup>, Eberhard Spiller<sup>2</sup>, Chris Walton<sup>2</sup>, and Guojing Zhang<sup>3</sup>

<sup>1</sup>Center for X-Ray Optics, Lawrence Berkeley National Laboratory, Berkeley, CA 94720

<sup>2</sup>EECS Department, University of California, Berkeley, CA 94720

<sup>2</sup>Lawrence Livermore National Laboratory, PO Box 808, Livermore, CA 94550

<sup>3</sup>Intel Corporation, 2200 Mission College Boulevard, Santa Clara CA 95052

## **Abstract**

Extreme ultraviolet lithography, the leading next-generation lithography candidate, has now entered the commercialization phase. One of the most daunting challenges to the commercial viability of this technology is the issue of defect-free multilayer-coated reflection masks. Of great potential interest are multilayer deposition processes that can effectively reduce the printability of substrate defects, thereby facilitating the precoating substrate-inspection task. In particular, ion-beam deposition with additional ion-assisted polishing has been shown to drastically reduce defect sizes as seen after multilayer coating. Here we report on tests performed to lithographically characterize the effectiveness of defect smoothing and to verify defect printability models. The results show that normally printable 50-nm substrate defects are rendered non-printable through the smoothing process. Moreover, a programmed defect fabrication method enabling controlled proximity printing tests is presented.

**Keyword:** extreme ultraviolet, lithography, multilayer, mask, defects

## Introduction

Extreme ultraviolet (EUV) lithography [1], the leading next-generation lithography candidate, has now entered the commercialization phase [2]. One of the most daunting challenges to the commercial viability of this technology is the issue of defect-free masks [3]. EUV systems are based on multilayer-coated [4] reflective components including both the projection optics and the mask. Defects below the multilayer (substrate defects) or embedded within the multilayer will be manifest as phase defects, thus even extremely small defect (smaller than the EUV wavelength) may, in principle, be printable.

Of great potential interest are multilayer deposition processes that can effectively reduce the printability of substrate defects, thereby facilitating the precoating substrate-inspection task. In particular, ion-beam deposition with additional ion-assisted polishing has been shown to drastically reduce defect sizes as seen after multilayer coating [5]. The effectiveness of this method has in the past been studied by depositing gold nanospheres on a surface and characterizing the post-coating surface topology using an atomic force microscope (AFM) [6]. Assumptions about the multilayer growth are then made to predict the effect of the defect on a reflected EUV field. The simplest of these assumptions treats the final defect as a pure phase structure where the phase is geometrically determined from the top surface profile [7].

Here we report on lithographic tests performed to further characterize the effectiveness of defect smoothing and to verify defect printability models. The tests were performed at the EUV microfield static exposure station [8] at Lawrence Berkeley National Laboratory's Advanced Light Source synchrotron radiation facility. In support of the tests, a new programmed-substrate-defect fabrication technique was developed enabling the programmed defects to be positioned in known

proximity to pattern features. Printing results show that the smoothing-optimized coatings do indeed significantly reduce the printability of substrate defects.

### **Fabrication of programmed substrate defects**

Crucial to the lithographic tests presented here was the fabrication of programmed substrate-defect masks. The relevant defect sizes on the substrate are on the order of  $50 \times 50 \times 50$  nm and, ideally, these defects are positioned controlled distances from absorber lines in order to test proximity effects. To address the fabrication issue, electron-beam lithography has been used to directly pattern a spin-on-glass resist (HSQ) [9]. The resist relief features remaining after processing, which take on the form of highly-robust silicon dioxide, serve as the programmed defects. This same technology has recently been used to fabricate high-efficiency reflective blazed-phase gratings operating at EUV wavelengths [10].

After fabrication of the defects onto standard 6-inch square  $\frac{1}{4}$ -inch thick mask substrates, the plates were multilayer coated at Lawrence Livermore National Laboratory. Two separate samples were coated, one employing the conventional ion-beam deposition method and a second employing the additional ion-assisted smoothing [5]. Subsequently, the absorber stack was deposited and electron-beam lithography again used to pattern the absorber layer. As for the defect exposure step, the pattern exposure was performed using Lawrence Berkeley National Laboratory's high-resolution electron-beam lithography tool [11] operating at 100 KeV. The overlay capabilities of this tool enabled patterning of the absorber layer with controlled proximity to the defects below the multilayer coating. Finally, the absorber stack etch process was performed at Intel corporation.

The mask layout included a variety of defect widths ranging from 50 nm to 140 nm all with heights of approximately 50 nm. Additionally, the layout included both proximity and isolated

defects. Here we report only on printing results from the more stringent proximity defect case. The proximity defects are embedded within a 6-bar pattern of 100-nm lines and spaces as printed in a clear field. The isolated defects were designed as 4×4 arrays of defects. Figure 1(a) shows the mask layout top view for a proximity defect field with 140-nm-wide centered defects and Fig. 1(b) shows a schematic stack view. The top-view regions in white represent the remaining absorber and the black regions are the exposed multilayer. The substrate defects, which are actually under the multilayer, are shown in dark gray. The complete mask layout includes a series of 6-bar patterns for each defect size where the defect spacing relative to the line pattern is varied and span a full period. This both enables the printability to be studied as a function of proximity and also significantly reduces the potential of overlay error between the defect and pattern layers.

Figure 2 shows an AFM image from one of the masks immediately following the defect layer fabrication. The image is of a subset of an isolated 50-nm 4×4 defect field. 50 nm refers to the lateral dimension of the defect, as noted above all the patterned defects were 50-nm tall. The large 2-um-wide feature, also patterned in HSQ, was added as a locating feature for the required pre- and post-coating AFM and scanning electron microscope (SEM) metrology. Because the AFM has limited spatial resolution, SEM analysis was also performed to validate the lateral dimensions of the patterned defects. Figure 3 shows a SEM image of one of the 50-nm patterned defects.

### **Characterization of the defects after coating**

As described above, two separate programmed defect masks were multilayer coated; one employing the conventional ion-beam deposition method and a second employing the additional ion-assisted smoothing [5]. The coated masks were again characterized by AFM before

implementing the absorber stack. Figure 4 shows AFM images of coated 50-nm-wide defects both with [Fig. 4(a)] and without [Fig. 4(b)] the additional smoothing process. With smoothing, the defect height is reduced to approximately 1 nm with a full-width at half maximum of 120 nm. Without smoothing, the defect height is approximately 15 nm with a width of 60 nm. Based on simple geometric phase approximations, it is evident that one would expect the 50-nm defect to print in the non-smoothing case and not print in the smoothing case [7].

Figure 5 shows a summary of the heights from various other AFM-characterized defects after coating. The plot shows the post-coating peak height as a function of defect width on the substrate. Again, we point out that all the defects were 50-nm tall on the substrate.

### **Lithographic printability test**

After completion of the of the absorber stack patterning, the masks were used in printing experiments at the EUV microfield static exposure station [8] at Lawrence Berkeley National Laboratory. This synchrotron-based system includes a programmable scanning illuminator allowing the illumination coherence conditions to be prescribed [12]. For the results presented here, disk illumination with a coherence factor ( $\sigma$ ) of 0.7 was used. The imaging optic was a 0.1-numerical aperture (NA), four-mirror, 4 $\times$ -reduction, lithographic optic [13]. This state-of-the-art optic [14] is the second of two optical systems fabricated as part of an industry consortium (the EUV LLC) effort developing EUV lithography in collaboration with Lawrence Berkeley, Lawrence Livermore, and Sandia National laboratories. This optic was temporally utilized at Berkeley for a variety of static printing tests including the defect-printability tests presented here. The optic was subsequently installed into the fully-functional EUV lithography engineering test stand (ETS), an alpha-class stepper [15].

The results presented here are based on proximity defects positioned at the center of the space. As stated above, line-space pattern is 100-nm at the wafer (400-nm on the mask). Defects widths ranging from 50 to 90 nm on the mask were analyzed. The analysis included both a dose range and focus range exceeding the  $\pm 10\%$  critical dimension (CD) change process window. Figure 6 shows a series of SEM images from prints of the proximity defects for both the smoothed [Fig. 6(a)] and unsmoothed [Fig. 6(b)] cases. These images were recorded at best focus and close to nominal dose (dose to size for the 100-nm lines). Where visible, the defect effects on the proximity line widths are circled. The label on each image represents the width in nm of the substrate defects on the mask.

Figure 7 shows a printability summary for a process latitude exceeding the  $\pm 10\%$  CD change process window. The printability is analyzed at nominal dose and  $\pm 10\%$  and through a focal range of  $\pm 1.2\ \mu\text{m}$  in  $0.6\text{-}\mu\text{m}$  steps. For reference, the process window size for 100-nm features is approximately  $2\text{-}\mu\text{m}$  depth of focus with a dose latitude of  $10\%$ . Each table represents one substrate defect size and coating condition. Each entry within each table represents the printability of the defect at the corresponding point in process space. For example, the central elements in the tables correspond to the best-focus, nominal-dose cases shown in Fig. 6. The defects are classified into three categories as a function of dose and focus:

- 1) **Light gray circle:** No measurable effect.
- 2) **Dark gray circle:** Measurable effect causing less than  $10\%$  line-width change to adjacent lines.
- 3) **Black circle:** Printable defect, measurable effect causing  $10\%$  or greater line-width change to adjacent lines. Because the defects considered here are defects centered in the space,  $10\%$  average adjacent line-width change corresponds to  $20\%$  space-width change.

From Fig. 7, it is evident that employing the defect-smoothing multilayer reduces the printable threshold for substrate defects from below 50 nm to about 60 nm. At 60 nm, the smoothed defect has a final height of approximately 1.7 nm. In comparison, the unsmoothed 50-nm defect has a height of approximately 15 nm. We note that one point is marked printable for the 50-nm smoothed case, however, this point is significantly beyond the defect-free CD-limited process window.

## **Discussion**

In closing, we compare the experimental results to those predicted based on the post-coating AFM measurements and the simplified top-surface geometric phase approximation [7]. The AFM-measured two-dimensional height profiles were used to determine the mask-plane phase error and aerial-image modeling was performed to generate the wafer-plane image. A simple binary resist model was assumed to determine the printed CD. Figure 8 shows a table similar to that in Fig. 7 but based on the aerial-image simulation data. In this case, measurable but not printable defects are those that cause greater than 5% and less than 10% CD change. This simple model is seen to be a good predictor of the printing results for the smoothing case but not for the unsmoothed case. This is to be expected because when the multilayer disturbance is very large, as is the case without smoothing, the defect will affect both amplitude (reflectivity) and phase. Under this condition, the modeling predicts worst results because the phase-shifted light will be predicted to have higher amplitude than is the case experimentally where the phase-shifted light is additionally attenuated.

The effectiveness of smoothing-optimized multilayers in reducing the printability of substrate defects has been demonstrated lithographically. To this end, a new programmed-defect fabrication method has been developed. Results show that with current smoothing multilayer technology, the

critical defect dimension on the mask is increased from below 50 nm to approximately 60 nm. We note, however, that these results were obtained from a 0.1-NA lithographic optic and that the printability of defects will increase with the NA (commercial EUV lithography tools are expected to have an NA of 0.25). The results presented here, however, do also validate modeling techniques that can be used to predict printability at these higher NAs.

The authors are greatly indebted to Kevin Bradley, Rene Delano, Paul Denham, Brian Hoef, Gideon Jones, Senajith Rekawa, and Ron Tackaberry for expert engineering and fabrication support, and to the entire CXRO staff for enabling this research. This research was supported by the Extreme Ultraviolet Limited Liability Company and carried out at Lawrence Berkeley National Laboratory under the auspices of the DOE Office of Basic Energy Science.

## References

1. R. Stulen and D. Sweeney, "Extreme ultraviolet lithography," IEEE J. Quantum Electron. **35**, 694-699 (1999).
2. H. Meiling, J. Benschop, R. Hartman, P. Kürz, P. Høghøj, R. Geyl, N. Harned, "EXSTATIC: ASML's  $\alpha$ -tool development for EUVL," Proc. SPIE **Vol. 4688**, 1-10 (2002).
3. S. Hector, "EUVL masks: requirements and potential solutions," Proc. SPIE **Vol. 4688**, 134-149 (2002).
4. J. H Underwood and T. W. Barbee, Jr., "Layered synthetic microstructures as Bragg diffractors for X rays and extreme ultraviolet: theory and predicted performance," Appl. Opt. **20**, 3027-3034 (1981).
5. P. Mirkarimi, E. Spiller, D. Stearns, S. Baker, V. Sperry, and E. Gullikson, "Developing a viable multilayer coating process for extreme ultraviolet lithography reticles" *in preparation*.



6. P. Mirkarimi, S. Baker, D. Stearns, "Technique employing gold nanospheres to study defect evolution in thin films," J. Vac. Sci. Technol. B **19**, 628-633 (2001).
7. E. Gullikson, C. Cerjan, D. Stearns, P. Mirkarimi, D. Sweeney, "Practical approach for modeling extreme ultraviolet lithography mask defects," J. Vac. Sci. Technol. B **20**, 81-86 (2002).
8. P. Naulleau, K. Goldberg, E. Anderson, D. Attwood, P. Batson, J. Bokor, P. Denham, E. Gullikson, B. Harteneck, B. Hoef, K. Jackson, D. Olynick, S. Rekawa, F. Salmassi, K. Blaedel, H. Chapman, L. Hale, P. Mirkarimi, R. Soufli, E. Spiller, D. Sweeney, J. Taylor, C. Walton, D. O'Connell, R. Stulen, D. Tichenor, C. Gwyn, P. Yan and G. Zhang, "Sub-70-nm EUV Lithography at the Advanced Light Source Static Microfield Exposure Station Using the ETS Set-2 Optic," J. Vac. Sci. & Technol. B, *to be published* (2002).
9. F. van Delft, J. Weterings, A. van Langen-Suurling, H. Romijn, "Hydrogen silsesquioxane/novolac bilayer resist for high aspect ratio nanoscale electron-beam lithography," J. Vac. Sci. Technol. B **18**, 3419-3423 (2000).
10. P. Naulleau, E. Anderson, E. Gullikson, and J. Bokor, "Fabrication of high-efficiency multilayer-coated binary blazed gratings in the EUV regime," Opt. Comm. **200**, 27-34 (2001).
11. E. H. Anderson, D. L. Olynick, B. Harteneck, E. Veklerov, Gregory Denbeaux, W. Chao, A. Lucero, L. Johnson, and D. Attwood, "Nanofabrication and diffractive optics for high-resolution x-ray applications," J. Vac. Sci. Technol. B **18**, 2970-2975 (2000).
12. P. Naulleau, K. Goldberg, P. Batson, J. Bokor, P. Denham, and S. Rekawa, "A Fourier-synthesis custom-coherence illuminator for EUV microfield lithography," Appl. Opt., *to be published* (2003).

13. D. W. Sweeney, R. Hudyma, H. N. Chapman, and D. Shafer, "EUV optical design for a 100 nm CD imaging system," in *Emerging Lithographic Technologies II*, Y. Vladimirsky, ed., Proc. SPIE **3331**, 2-10 (1998).
14. K. Goldberg, P. Naulleau, J. Bokor, and H. Chapman, "Honing the accuracy of extreme ultraviolet optical system testing: at-wavelength and visible-light measurements of the ETS Set-2 projection optic," Proc. SPIE Vol. **4688**, 329-337 (2002).
15. D. Tichenor, A. Ray-Chaudhuri, S. Lee, H. Chapman, W. Replogle, K. Berger, R. Stulen, G. Kubiak, L. Klebanoff, J. Wronosky, D. O'Connell, A. Leung, K. Jefferson, W. Ballard, L. Hale, K. Blaedel, J. Taylor, J. Folta, E. Spiller, R. Soufli, G. Sommargren, D. Sweeney, P. Naulleau, K. Goldberg, E. Gullikson, J. Bokor, D. Attwood, U. Mickan, R. Hanzen, E. Panning, P. Yan, J. Bjorkholm, and C. Gwyn, "Initial Results from the EUV Engineering Test Stand," Proc. SPIE Vol. **4506**, 639-645 (2001).

5. P. Mirkarimi, E. Spiller, D. Stearns, V. Sperry, S. Baker, “An ion-assisted Mo-Si deposition process for planarizing reticle substrates for extreme ultraviolet lithography,” *IEEE J. Quantum Electron.* **37**, 1514-1516 (2001).

## 16. List of Figures

**Fig. 1.** Mask layout top view(a) for a 140-nm proximity defect field and schematic stack view (b). The top-view regions in white represent the remaining absorber and the black regions are the exposed multilayer. The substrate defects, which are actually under the multilayer, are shown in dark gray.

**Fig. 2.** AFM image from one of the masks immediately following the defect layer fabrication. The image is from a subset of an isolated 50-nm 4×4 defect field. 50 nm refers to the lateral dimension of the defect, all the patterned defects were 50-nm tall. The large 2-um-wide feature, also patterned in HSQ, was added as a locating feature for the required pre- and post-coating AFM and scanning electron microscope (SEM) metrology.

**Fig. 3.** SEM image of one of the 50-nm patterned defects from Fig. 2.

**Fig. 4.** AFM images of coated 50-nm-wide defects after multilayer coating both with (a) and without (b) the additional smoothing process.

**Fig. 5.** Summary of defect heights after multilayer coating based on AFM measurement. The plot shows the post-coating peak height as a function of defect width on the substrate. All the defects were 50-nm tall on the substrate.

**Fig. 6.** SEM images from prints of the proximity defects for defect widths ranging from 50 nm to 90 nm for both the smoothed (a) and unsmoothed (b) cases. These images were recorded at best focus and close to nominal dose. Where visible, the defect effects on the proximity line widths are circled.

**Fig. 7.** Defect printability summary over a process latitude exceeding the  $\pm 10\%$  CD change process window. The printability is analyzed at nominal dose and  $\pm 10\%$  and through a focal range of  $\pm 1.2 \mu\text{m}$  in  $0.6\text{-}\mu\text{m}$  steps. For reference, the process window size for 100-nm features is

approximately 2- $\mu\text{m}$  depth of focus with a dose latitude of 10%. Each table represents one substrate defect size and coating condition. Each entry within each table represents the printability of the defect at the corresponding point in process space.

**Fig. 8.** Table similar to that in Fig. 7 but based on the aerial-image simulation data using the top-surface geometric phase approximation. In this case, measurable but not printable defects are those that cause greater than 5% and less than 10% CD change. This simple model is seen to be a good predictor of the printing results for the smoothing case but not for the unsmoothed case. This is to be expected because when the multilayer disturbance is very large, as is the case without smoothing, the defect will affect both amplitude (reflectivity) and phase.

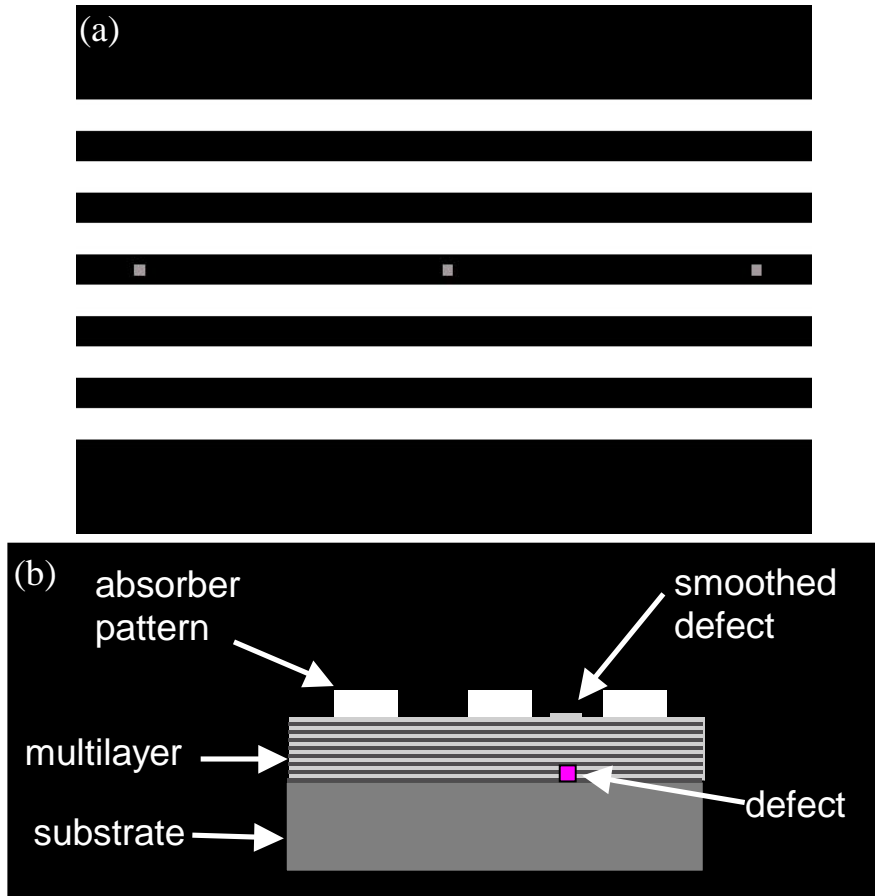


**Fig. 1.** Mask layout top view(a) for a 140-nm proximity defect field and schematic stack view (b). The top-view regions in white represent the remaining absorber and the black regions are the exposed multilayer. The substrate defects, which are actually under the multilayer, are shown in dark gray.

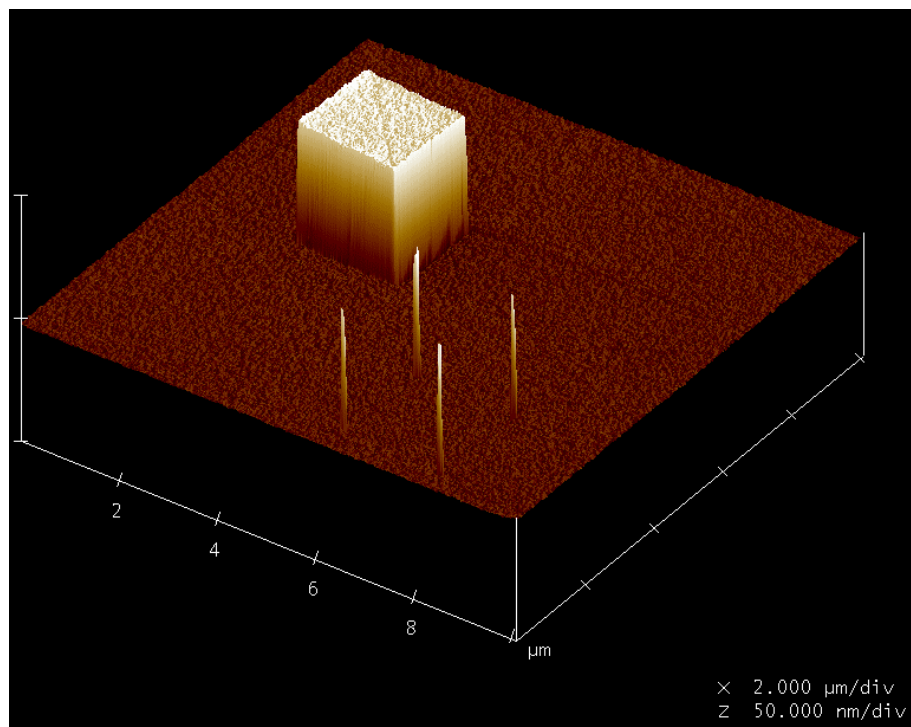


**Fig. 2.** AFM image from one of the masks immediately following the defect layer fabrication. The image is from a subset of an isolated 50-nm  $4\times 4$  defect field. 50 nm refers to the lateral dimension of the defect, all the patterned defects were 50-nm tall. The large 2- $\mu$ m-wide feature, also patterned in HSQ, was added as a locating feature for the required pre- and post-coating AFM and scanning electron microscope (SEM) metrology.

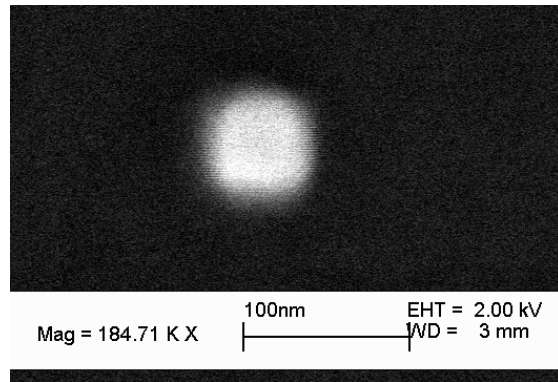


**Fig. 3.** SEM image of one of the 50-nm patterned defects from Fig. 2.



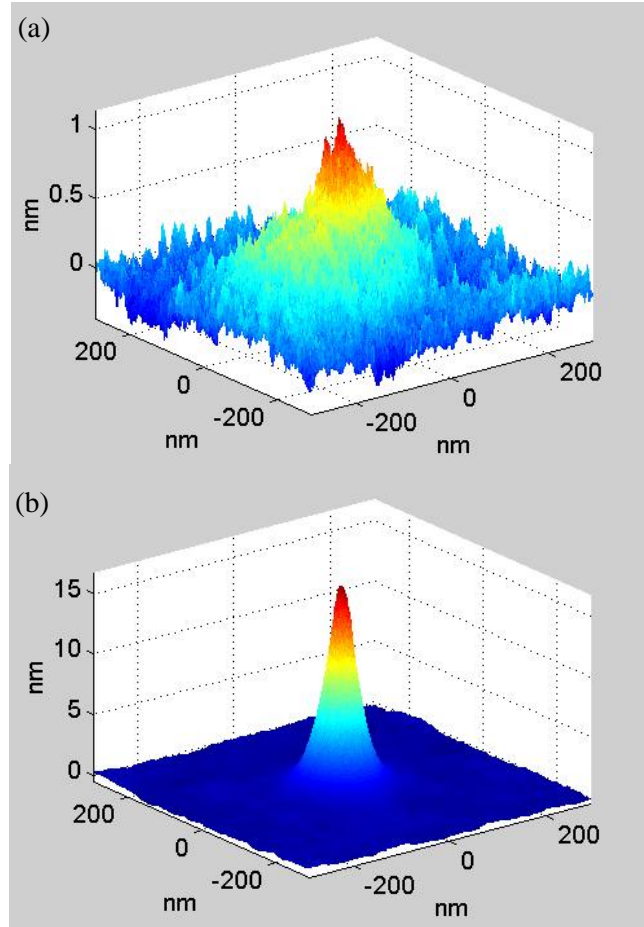


**Fig. 4.** AFM images of coated 50-nm-wide defects after multilayer coating both with (a) and without (b) the additional smoothing process.

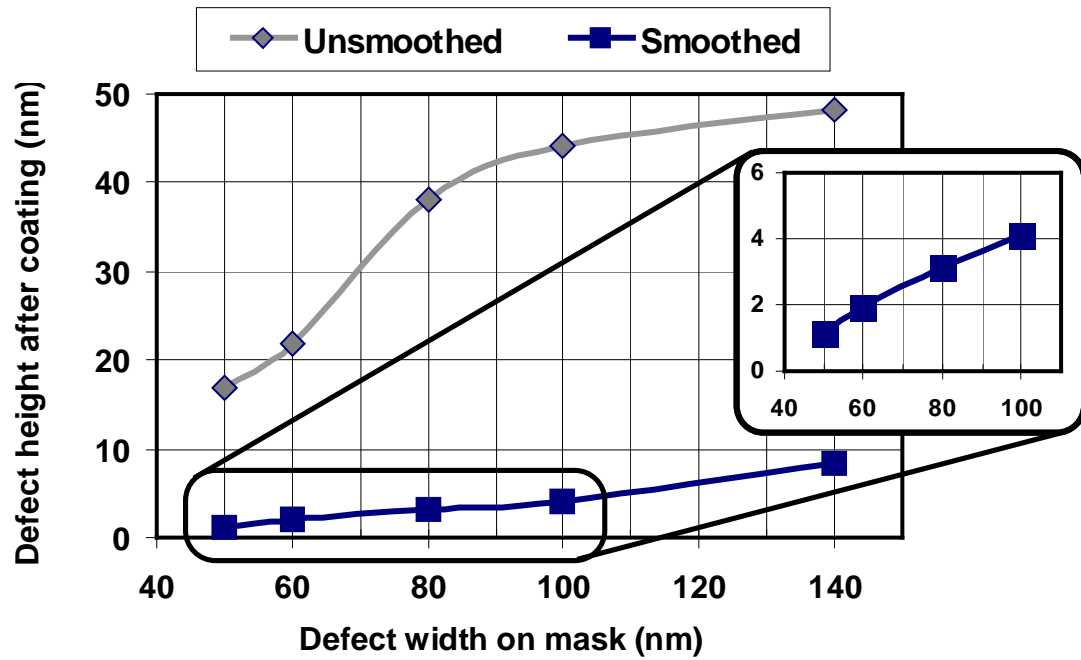


**Fig. 5.** Summary of defect heights after multilayer coating based on AFM measurement. The plot shows the post-coating peak height as a function of defect width on the substrate. All the defects were 50-nm tall on the substrate.

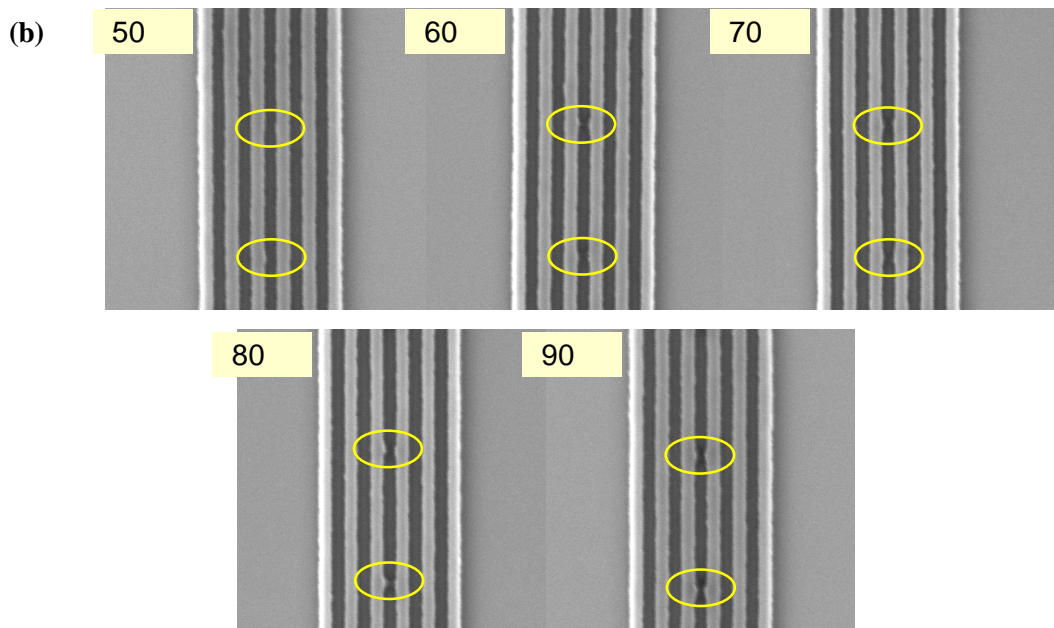
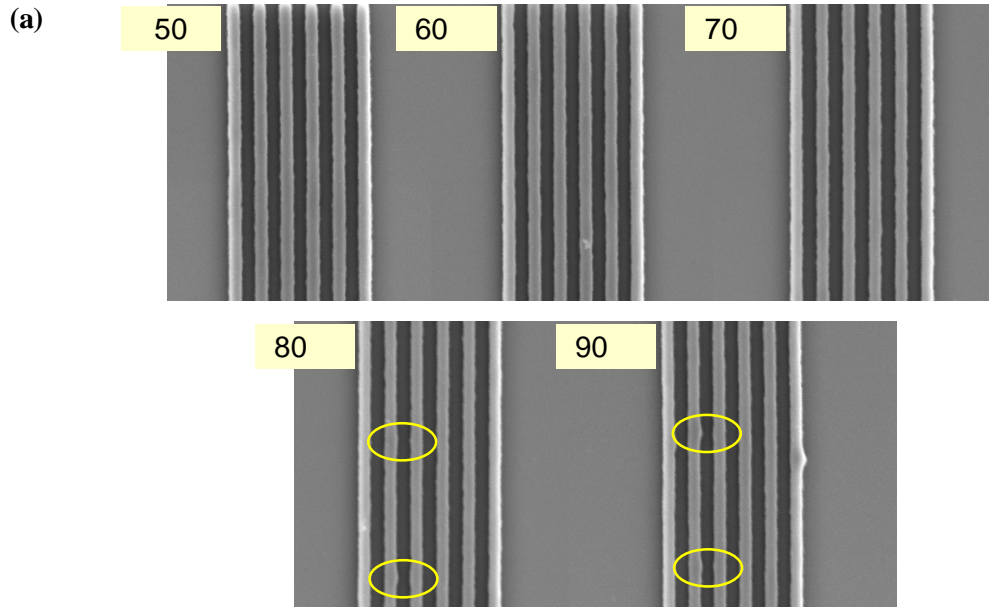


**Fig. 6.** SEM images from prints of the proximity defects for defect widths ranging from 50 nm to 90 nm for both the smoothed (a) and unsmoothed (b) cases. These images were recorded at best focus and close to nominal dose. Where visible, the defect effects on the proximity line widths are circled.

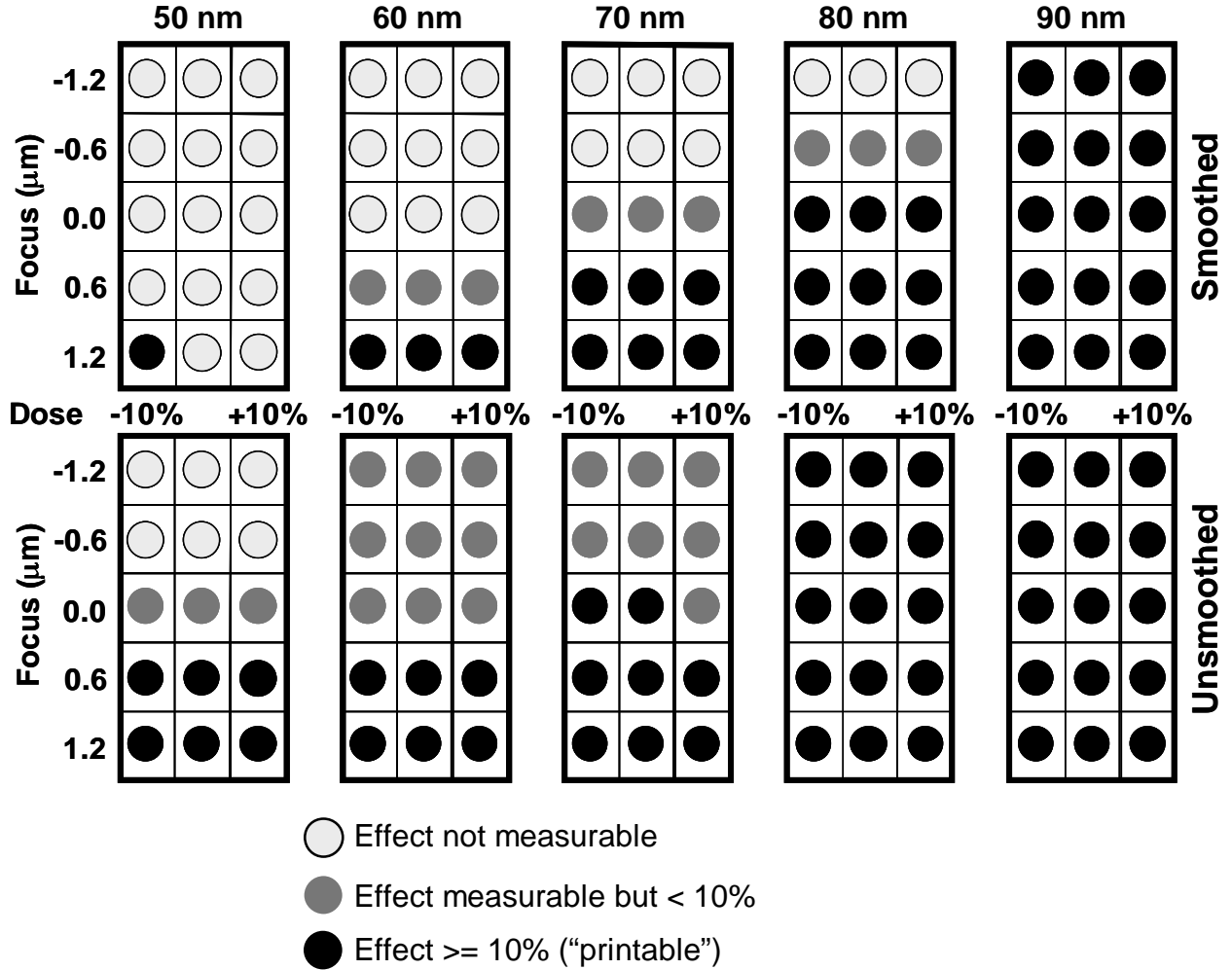


**Fig. 7.** Defect printability summary over a process latitude exceeding the  $\pm 10\%$  CD change process window. The printability is analyzed at nominal dose and  $\pm 10\%$  and through a focal range of  $\pm 1.2 \mu\text{m}$  in  $0.6\text{-}\mu\text{m}$  steps. For reference, the process window size for 100-nm features is approximately  $2\text{-}\mu\text{m}$  depth of focus with a dose latitude of 10%. Each table represents one substrate defect size and coating condition. Each entry within each table represents the printability of the defect at the corresponding point in process space.

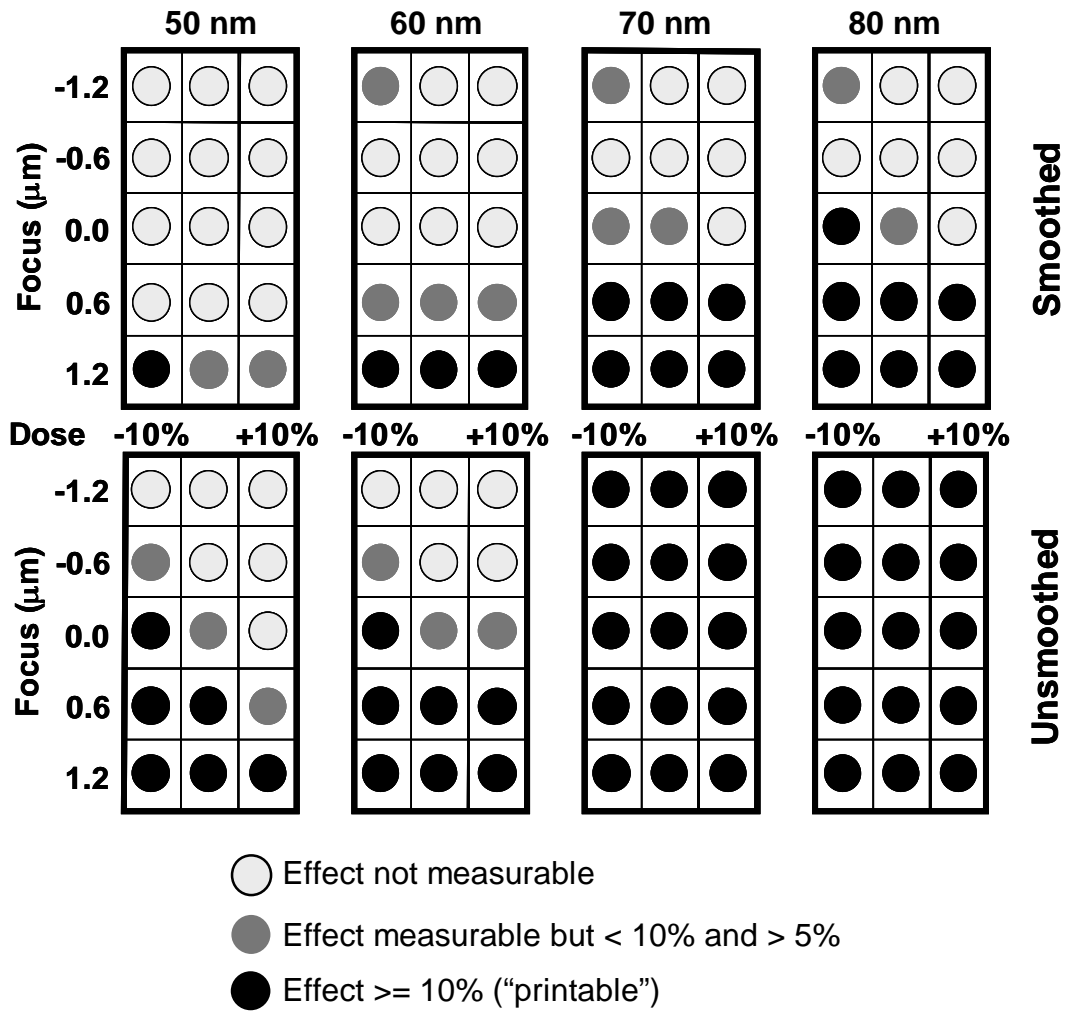


**Fig. 8.** Table similar to that in Fig. 7 but based on the aerial-image simulation data using the top-surface geometric phase approximation. In this case, measurable but not printable defects are those that cause greater than 5% and less than 10% CD change. This simple model is seen to be a good predictor of the printing results for the smoothing case but not for the unsmoothed case. This is to be expected because when the multilayer disturbance is very large, as is the case without smoothing, the defect will affect both amplitude (reflectivity) and phase.